

Superresolution Planar Diffraction Tomography through Evanescent Fields

Sean K. Lehman

Lawrence Livermore National Laboratory, Livermore, CA 94550. E-mail: lehman2@llnl.gov

Received 13 March 2001; accepted 23 October 2001

ABSTRACT: We consider the problem of noninvasively locating objects buried in a layered medium such as land mines in the ground or objects concealed in a wall. In such environments, the transmitter(s) and receiver(s) are frequently within the near-field region of the illuminating radiation. In these cases, the scattered evanescent field carries useful information on the scattering object. Conventional diffraction tomography techniques neglect, by their design, the evanescent field. Under near-field conditions, they treat it as noise as opposed to valid data. If correctly incorporated into a reconstruction algorithm, the evanescent field, which carries high spatial frequency information, can be used to achieve resolution beyond the classical limit of $\lambda/2$, or “superresolution.” We build on the generalized holography theory presented by Langenberg to develop a planar diffraction tomography algorithm that incorporates evanescent field information to achieve superresolution. Our theory is based on a generalization of the Fourier transform, which allows for complex spatial frequencies in a manner similar to the Laplace transform. We specialize our model to the case of a two-dimensional multimono-static, wideband imaging system, and derive an extended resolution reconstruction procedure. We implement and apply our reconstruction to two data sets collected using the Lawrence Livermore National Laboratory (LLNL) Micropower Impulse Radar (MIR). © 2002 John Wiley & Sons, Inc. *Int J Imaging Syst Technol*, 12, 16–26, 2002; DOI 10.1002/ima.10006

I. INTRODUCTION

We consider the problem of noninvasively locating objects buried or otherwise concealed in a layered medium such as land mines in the ground or objects hidden in a wall (Fig. 1). In noninvasive wave (either electromagnetic or acoustic wave) probing of layered media in near-field conditions, few researchers outside of optical microscopists have taken advantage of the evanescent part of the scattered field to enhance resolution. The evanescent field contains high spatial frequency information, i.e., spatial frequency information beyond the “classical” diffraction limit of $\lambda/2$ (Born and Wolf, 1999). Thus, if correctly used in a tomographic reconstruction algorithm, resolution beyond the diffraction limit, or equivalently “superresolution,” can be achieved.

Expanding the theory presented by Langenberg (1987), we propose and develop a diffraction tomographic (Devaney, 1982) reconstruction technique to be used in near-field environments. The technique achieves superresolution by including the evanescent part of the field backscattered from objects buried in a layered medium. Most diffraction tomography reconstruction algorithms (André et al., 1995, 1997; Devaney, 1982; Kak and Slaney, 1988; Mast, 1993) are band limited to the classical resolution limit. Two reasons account for this: (1) They operate in the far field where the high spatial frequencies have been lost due to propagation effects and (2) including the higher spatial frequencies into the algorithms is difficult due to their exponentially decaying nature. Most methods employed to achieve superresolution use “after-the-fact” techniques, i.e., they use a priori information (such as models, or constraints on the data) to extract more information from data that have already been collected (Hunt, 1995). The method described here is to design reconstruction algorithms that use the higher spatial frequencies during the reconstruction. Schatzberg and Devaney (1992a, b) developed the first diffraction tomographic reconstruction algorithm that explicitly includes the evanescent field. Building on Devaney’s diffraction tomography work, Bohbot et al. (1994) developed a superresolution eddy current imaging algorithm in metal half-planes. Deming (1996) and Deming and Devaney (1997) developed an electromagnetic diffraction tomography reconstruction algorithm for a half-plane medium that uses the full spectrum of the measured scattered fields to achieve superresolution. Additionally, it models the physical scattering characteristics of the transmitting and receiving antennas. Full wave methods (Berggren et al., 1986a, b; Bolomey and Pichot, 1990; Dorn et al., 1999; Joachimowicz et al., 1991; Johnson and Tracy, 1983; Natterer and Wubbeling, 1995; Wiskin et al., 1997) implicitly incorporate the evanescent field component because they attempt to invert the full wave equation.

Section II summarizes the theory behind the far-field forward scattering models, which do not include the evanescent field. In Section III, we present our “total field” scattering model, which includes the evanescent field. In Sections II and III, we specialize the model to a planar multimono-static environment. It is evident, when comparing the two models, that the far-field model does not contain the evanescent field whereas the total field model does.

This work was performed under the auspices of the U.S. Department of Energy by University of California Lawrence Livermore National Laboratory under contract No. W-7405-Eng-48.

Correspondence to: Sean K. Lehman

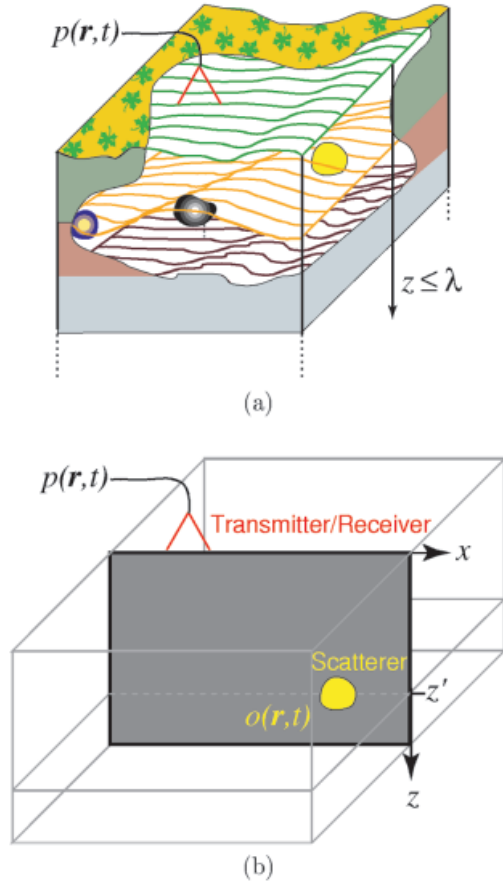


Figure 1. Layered medium problem scenario. (a) We want to determine noninvasively the location and nature of objects buried in a layered medium and residing within the near field of the radiation. (b) 2D simplification. A scattering object $o(\mathbf{r}, t)$ is buried in a medium. A transmitter/receiver launches a pulse $p(\mathbf{r}, t)$ into the medium and records the echo from the scatterer.

Section IV presents the inversion algorithm for a wideband incident field operating in a reflection mode. Our algorithm requires the use of a spatial frequency domain filter to limit the exponentially

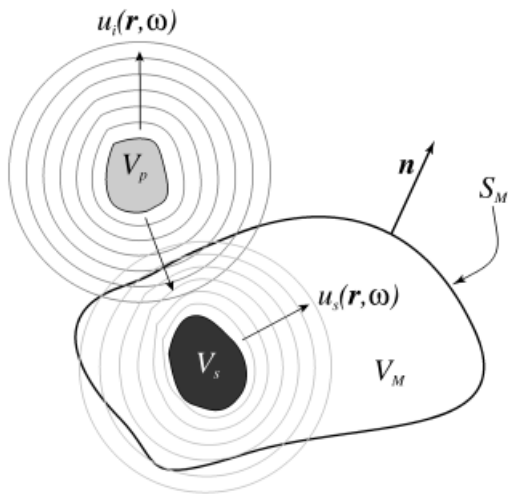


Figure 2. Model of a wave probing system.

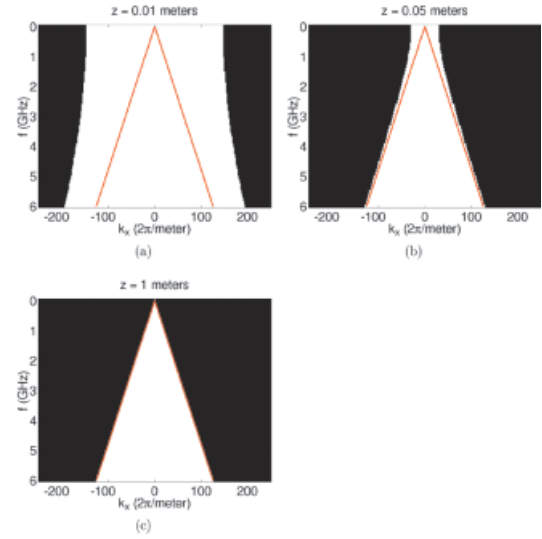


Figure 3. Evanescent cutoff windows. Examples of the evanescent cutoff windows as a function of wavenumber and frequency for three values of z . (a) $z = .01$ m. (b) $z = .05$ m. (c) $z = 1$ m.

diverging evanescent field. For comparison, we include a far-field reconstruction algorithm that does not make use of the evanescent field. Section V consists of a proof-of-principle using scattering from two point sources under the Born approximation. In Section VI, we apply the reconstruction algorithms to real, wideband radar measurements using the Lawrence Livermore National Laboratory (LLNL) Micropower Impulse Radar (MIR). The reconstruction results show increased resolution and contrast when compared with a standard diffraction tomography reconstruction algorithm. Conclusions are presented in Section VII.

II. PORTER-BOJARSKI EQUATION

We summarize the derivation of the Porter-Bojarski equation, the most common forward scattering model, and immediately specialize it to the multimono-static case using frequency diversity. That is, we use multiple frequencies to achieve spatial spectral coverage as opposed to multiple views.

The Porter-Bojarski equation (Langenberg, 1987; Lehman, 2000) represents the forward scattering model in a far-field propagation tomography measurement system. In Figure 2, a measurement surface, S_M , encloses the volume, V_M , containing a scattering object occupying V_s . The primary source, occupying V_p , lies outside of V_M . It launches the incident probing field, $u_i(\mathbf{r}, \omega)$, which propagates into V_M and interacts with the scattering object creating the scattered field, $u_s(\mathbf{r}, \omega)$. The scattered field is measured on the measurement surface and serves as the data to be backpropagated during the reconstruction procedure.

The Porter-Bojarski equation is derived from a generalized, time-reversed description of the total field within the volume. Porter and Bojarski define the generalized field inside the measurement volume (Langenberg, 1987)

$$\chi(\mathbf{r}, \omega) \equiv \oint_{S_M} dS' [G^*(\mathbf{r} - \mathbf{r}', \omega) \partial_n u(\mathbf{r}', \omega) - u(\mathbf{r}', \omega) \partial_n G^*(\mathbf{r} - \mathbf{r}', \omega)], \quad (1)$$

where $G^*(\mathbf{r}, \omega)$ is the complex conjugate of the free-space Green's function, $\partial_n u(\mathbf{r}, \omega) \equiv \mathbf{n} \cdot \nabla u(\mathbf{r}, \omega)$, \mathbf{n} is the outward normal to V_M as indicated in Figure 2, and $u(\mathbf{r}, \omega)$ is the total field within the measurement volume.

Through the application of Green's theorem, Eq. (1) reduces to (Langenberg, 1987; Lehman, 2000)

$$\oint_{S_M} dS' [G^*(\mathbf{r} - \mathbf{r}', \omega) \partial_n u_s(\mathbf{r}', \omega) - u_s(\mathbf{r}', \omega) \partial_n G^*(\mathbf{r} - \mathbf{r}', \omega)] \\ = 2ik_0^2(\omega) \int_{V_M} d\mathbf{r}' G_{im}(\mathbf{r} - \mathbf{r}', \omega) u(\mathbf{r}', \omega) o(\mathbf{r}', \omega), \quad (2)$$

where $G_{im}(\mathbf{r}, \omega)$ is the imaginary part of the Green's function and $o(\mathbf{r}, \omega)$ is the unknown scattering object to be determined. The surface integral on the left-hand side of Eq. (2) contains the known scattered field on the measurement surface. Equation (2) is the Porter-Bojarski equation. It provides a far-field relationship between the unknown object and the measured scattered field. We use the term "far-field" in the sense that the Porter-Bojarski equation contains no evanescent field component (Lehman, 2000).

When the total field in the right-hand side integrand of Eq. (2) is replaced by the incident field, i.e., when the Born approximation (Born and Wolf, 1999) is used, and the equation is specialized to a planar wave probing system with a planar incident field, it reduces to the Fourier diffraction theorem (Kak and Slaney, 1988), which relates the planar Fourier transform of the scattered field measured on a plane to the full Fourier transform of the object,

$$O(\mathbf{k}_\perp, k_0(\omega) \mp \gamma(\mathbf{k}_\perp, \omega), \omega) = \mp \frac{i\gamma(\mathbf{k}_\perp, \omega) e^{\mp i\gamma(\mathbf{k}_\perp, \omega) z_M}}{2k_0^2(\omega) A(\omega)} \\ \times \bar{U}_s(\mathbf{k}_\perp, z_M, \omega) S(k_0(\omega) - |\mathbf{k}_\perp|), \quad (3)$$

where $\mathbf{k}_\perp \equiv (k_x, k_y)$ is the planar Fourier wave vector, O is the spatial Fourier transform of the object, $\bar{U}_s(\mathbf{k}_\perp, z_M, \omega)$ is the planar Fourier transform of the measured field along the measurement surface described by $z = z_M$, a constant, ω is the temporal frequency, $k_0(\omega) \equiv \omega/c$ is the background wavenumber, and $\gamma(\mathbf{k}_\perp, \omega) \equiv \sqrt{k_0^2(\omega) - |\mathbf{k}_\perp|^2}$ with the branch of the square root chosen to make $\text{Im}\{\gamma(\mathbf{k}_\perp, \omega)\} > 0$. $A(\omega)$ is the Fourier amplitude of the incident field at frequency ω . The \pm sign choice depends on the mode of operation, which may be transmission (+) or reflection (-). $S(k)$ is the unit step function. It appears naturally within the derivation of Eq. (3) and explicitly suppresses spatial frequencies for which $|\mathbf{k}_\perp| > k_0(\omega)$, i.e., the evanescent field. For this derivation, we defined planar Fourier transform of the measured scattered field as

$$\bar{U}_s(\mathbf{k}_\perp, z_M, \omega) \equiv \int d\mathbf{r}_\perp u_s(\mathbf{r}_\perp, z_M, \omega) e^{i\mathbf{k}_\perp \cdot \mathbf{r}_\perp}, \quad (4)$$

where $\mathbf{r}_\perp \equiv (x, y)$ is the planar Cartesian coordinate.

III. TOTAL FIELD SCATTERING MODEL

Wishing to develop a forward scattering model that includes both propagating and evanescent field components, we proposed and proved (Lehman, 2000) a total field model for the field within the

measurement volume that includes both propagating and evanescent field components:

$$u(\mathbf{r}, \omega) = k_0^2(\omega) \int_{V_M} d\mathbf{r}' G^*(\mathbf{r} - \mathbf{r}', \omega) u(\mathbf{r}', \omega) o(\mathbf{r}', \omega) + \oint_{S_M} dS' \\ \times [G^*(\mathbf{r} - \mathbf{r}', \omega) \partial_n u(\mathbf{r}', \omega) - u(\mathbf{r}', \omega) \partial_n G^*(\mathbf{r} - \mathbf{r}', \omega)]. \quad (5)$$

Through the application of Green's theorem to Eq. (5), we obtain a relationship between the scattered field and the unknown object function:

$$u_s(\mathbf{r}, \omega) - \oint_{S_M} dS' [G^*(\mathbf{r} - \mathbf{r}', \omega) \partial_n u_s(\mathbf{r}', \omega) \\ - u_s(\mathbf{r}', \omega) \partial_n G^*(\mathbf{r} - \mathbf{r}', \omega)] \\ = k_0^2(\omega) \int_{V_M} d\mathbf{r}' G^*(\mathbf{r} - \mathbf{r}', \omega) u(\mathbf{r}', \omega) o(\mathbf{r}', \omega). \quad (6)$$

When specialized to a multimono-static planar environment under the Born approximation, Eq. (6) reduces to (Lehman, 2000)

$$\int dz' \bar{O}(\mathbf{k}_\perp, z', \omega) e^{i(k_0(\omega) \pm \gamma^*(\mathbf{k}_\perp, \omega))z'} \\ = \frac{i4\pi\gamma^*(\mathbf{k}_\perp, \omega)[1 \pm 0.5S(k_0(\omega) - |\mathbf{k}_\perp|)] e^{\pm i\gamma^*(\mathbf{k}_\perp, \omega)z_M}}{k_0^2(\omega)A(\omega)} \bar{U}_s(\mathbf{k}_\perp, z_M, \omega). \quad (7)$$

We interpret the z' -integral as being a generalized Fourier transform that allows for complex spatial frequencies. Defining the generalized Fourier transform of the object function to be

$$O(\mathbf{k}_\perp, -k_0(\omega) \pm \gamma^*(\mathbf{k}_\perp, \omega)) \equiv \int dz' \bar{O}(\mathbf{k}_\perp, z', \omega) e^{i(-k_0(\omega) \pm \gamma^*(\mathbf{k}_\perp, \omega))z'}, \quad (8)$$

we express Eq. (7) as

$$O(\mathbf{k}_\perp, -k_0(\omega) \pm \gamma^*(\mathbf{k}_\perp, \omega)) \\ = \frac{i4\pi\gamma^*(\mathbf{k}_\perp, \omega)[1 \pm 0.5S(k_0(\omega) - |\mathbf{k}_\perp|)] e^{\pm i\gamma^*(\mathbf{k}_\perp, \omega)z_M}}{k_0^2(\omega)A(\omega)} \bar{U}_s(\mathbf{k}_\perp, z_M, \omega). \quad (9)$$

In the total field case, the evanescent field component is no longer suppressed. The unit step function that had limited the measured field spectrum to the propagating regions in Eq. (3) now appears, reduced by a half and summed with one. The object spectrum on the left-hand side exists within the generalized Fourier space defined by Eq. (8), which allows for complex spatial frequencies.

We derive the inverse to Eq. (9), for the two-dimensional (2D) case, in Lehman (2000) and show it to be

$$o_{xr}(x, z) = \frac{1}{2\pi^2 v_0} \int_0^\infty d\omega \frac{e^{ik_0(\omega)z}}{k_0^2(\omega)A(\omega)} \int dk_x i^{S(k_0(\omega)-|k_x|)} \times [1 \pm 0.5S(k_0(\omega) - |k_x|)] - \gamma^*(k_x, \omega) \pm k_0(\omega) | \bar{U}_s(k_x, z_M, \omega) e^{-ik_{xx}} e^{\mp i\gamma^*(k_x, \omega)(z-z_M)}, \quad (10)$$

where v_0 is the background wave velocity, and where we use the xr subscript to indicate this is an extended resolution reconstruction that incorporates evanescent spatial frequencies. Care must be taken when implementing Eq. (10) as the expression $e^{\mp i\gamma^*(k_x, \omega)(z-z_M)}$ diverges as $|k_x| \rightarrow \infty$, i.e., within the evanescent region. The reason is that we are inverting exponentially decreasing field information. In the next section, we numerically implement Eq. (10). In doing so, we limit the extent of the k_x -integral by imposing a planar cutoff beyond which we assume the measured planar field spectrum, $\bar{U}_s(k_x, z_M, \omega)$, has no valid information, i.e., it has exponentially decreased to the point where there is no information. This cutoff in k_x is a function of z , the distance we have backpropagated the field. We may view this transition as when the signal information has dropped below the noise floor.

Equation (10) represents a reconstruction of the unknown object using the measured planar field spectrum. As it includes evanescent field information, we achieved our goal of developing a reconstruction procedure that extends the resolution beyond the classical resolution limit. In the next section, we discuss the numerical implementation of the reconstruction algorithm.

IV. INVERSION ALGORITHM

For comparison, we implemented two versions of the wideband planar multimono-static inversion algorithms: a strictly low pass code using exclusively the measured propagating fields and our extended resolution code using both propagating and evanescent fields. The low pass code implements a discrete representation of

$$o_{lp}(x, z) = \frac{i}{2\pi^2 v_0} \int_0^\infty d\omega \frac{e^{ik_0(\omega)z}}{k_0^2(\omega)A(\omega)} \int_{|k_x| \leq k_0(\omega)} dk_x |\gamma(k_x, \omega) + k_0(\omega) | \bar{U}_s(k_x, 0, \omega) e^{-ik_{xx}} e^{i\gamma(k_x, \omega)z}, \quad (11)$$

where we designate the low pass reconstruction with the lp subscript. Our extended resolution code implements a discrete representation of

$$o_{xr}(x, z) = \frac{1}{2\pi^2 v_0} \int_0^\infty d\omega \frac{e^{ik_0(\omega)z}}{k_0^2(\omega)A(\omega)} \times \int dk_x i^{S(k_0(\omega)-|k_x|)} |\gamma^*(k_x, \omega) + k_0(\omega) | M(k_x, z, \omega) \bar{U}_s(k_x, 0, \omega) e^{-ik_{xx}} e^{i\gamma^*(k_x, \omega)z}, \quad (12)$$

where the xr subscript indicates extended resolution. We explicitly set the location of the measurement plane, z_M , to zero.

We note the inclusion of the $M(k_x, z, \omega)$ function in the equation. This is a cutoff window that limits the extent of the evanescent field information used in the reconstruction. It serves the dual purpose of limiting the exponential expression $e^{i\gamma^*(k_x, \omega)z}$, which diverges in the evanescent region, and setting the limit beyond which no object spectral information is contained in the measured planar field spectrum. In the evanescent region, the object's planar spectral information decreases exponentially and will

pass below the noise threshold at some point in the measured planar spectrum. We define the limit beyond which the measured planar spectrum contains no objective information as the planar wavenumber cutoff or k_{xc} .

In the algorithm, this limit is specified in terms of the exponential decay of the forward model in the evanescent region. Within the evanescent region, it relates the amount of decay to the wavenumber cutoff via

$$e^{-\sqrt{k_{xc}^2 - k_0^2(\omega)}z_c} = \tau, \quad (13)$$

where τ is the selected fractional decay and z_c is the cutoff distance beyond which the evanescent field information has decayed to the point where it is unusable. That is, the field has decayed below the noise floor or is simply zero. For wavenumbers exceeding k_{xc} , evanescent fields should not be used in the reconstruction. We wish to relate k_{xc} to z_c as this governs how much evanescent information can be used as the reconstruction backpropagates away from the receiver. Solving Eq. (13) for k_{xc} in terms of distance from the receiver, we find

$$k_{xc}(z) = \sqrt{\left(\frac{1}{z} \ln \tau\right)^2 + k_0^2(\omega)}. \quad (14)$$

Equation (14) specifies *how much evanescent information can be used in the reconstruction after having backpropagated a distance z from the receiver*. As the reconstruction plane moves farther from the receiver, less evanescent information can be used. As we move into the far field, the wavenumber cutoff reduces to the propagating limit:

$$\lim_{z \rightarrow \infty} k_{xc}(z) = k_0(\omega). \quad (15)$$

Given the wavenumber cutoff, $k_{xc}(z)$, the cutoff window, $M(k_x, z, \omega)$, in Eq. (12) is simply a step function:

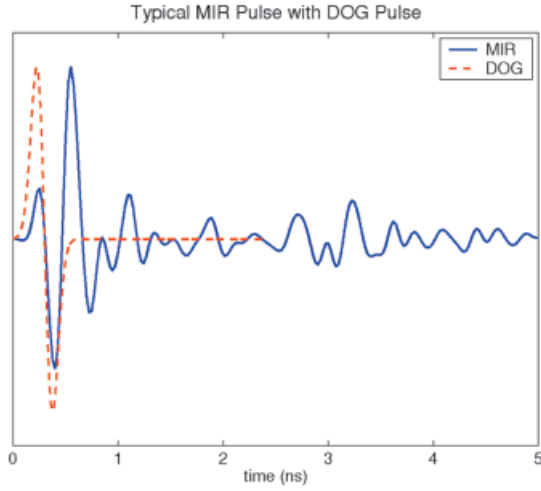
$$M(k_x, z, \omega) \equiv S(k_{xc}(z) - |k_x|), \quad (16)$$

where $S(x)$ is the unit step function. Examples of this window are shown in Figure 3 for three values of z : .01 m, .05 m, and 1 m. The lines forming an inverted “V” superposed on each figure delimit the propagating wavenumber cutoff of $k_0(\omega)$. As z increases, the pass band of the window collapses to the propagating region.

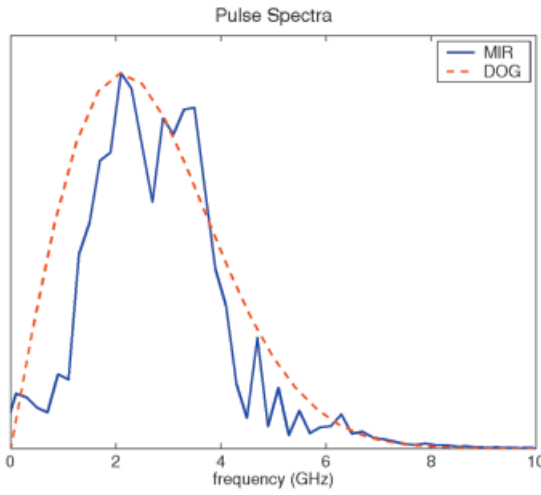
A final comment must be made on the division of the incident pulse spectrum, $A(\omega)$, in the reconstruction equations of Eqs. (11) and (12). A division in the temporal frequency domain corresponds to a deconvolution in the time domain. Thus, the division of the incident pulse spectrum is known as incident pulse deconvolution. No special care was taken in our numerical implementation of the incident pulse deconvolution. We simply divided by $A(\omega)$, but specialized techniques exist to perform this task (Carter, 1993) (particularly when $A(\omega)$ is zero).

V. PROOF-OF-PRINCIPLE

As a proof-of-principle and in order to confirm basic code operation, we analytically simulated the received field from two point scatterers under the Born approximation. The model for the scattered field is

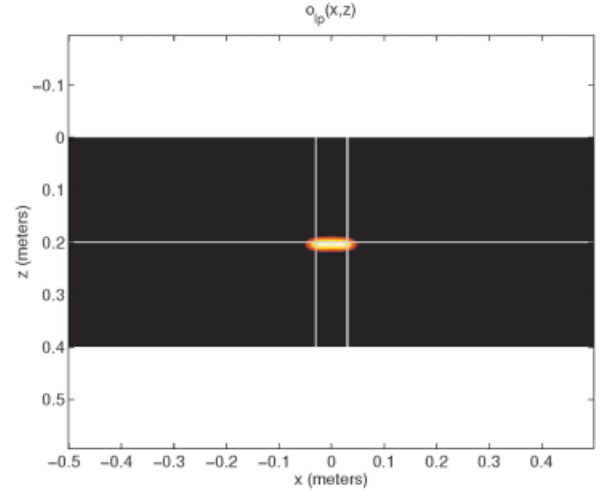


(a)

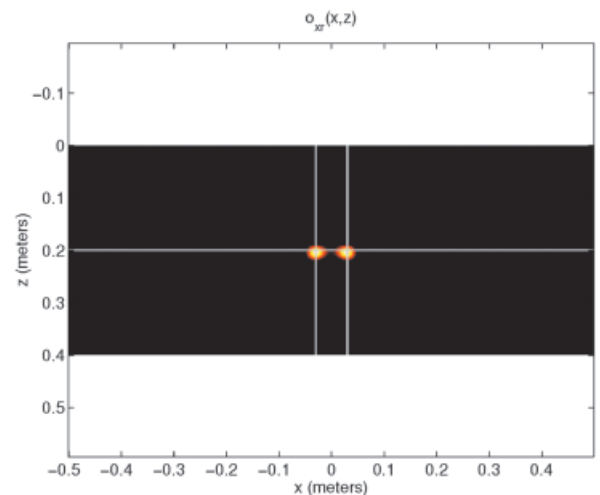


(b)

Figure 4. LLNL MIR pulse and DOG model. (a) Time domain pulses. (b) Pulse spectra.



(a)



(b)

Figure 6. Two-point scatterer reconstruction. (a) Low pass reconstruction. (b) Extended resolution reconstruction.

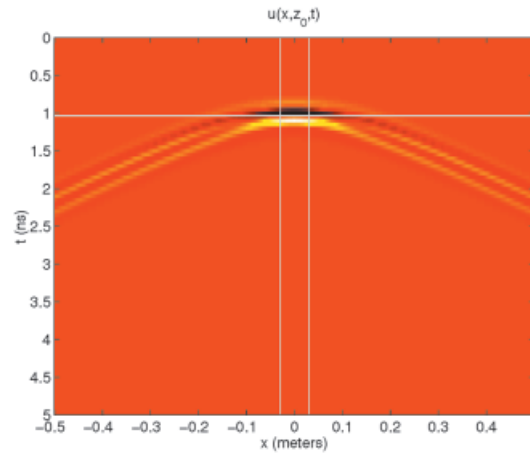


Figure 5. Two-point scatterer field. The scatterers are separated by 6 cm and are 20 cm from the source/measurement line at $z_0 = z_M = 0$. The scatterer locations are indicated by the cross hairs.

$$u_s(\mathbf{r}, \omega) = k_0^2(\omega) \int d\mathbf{r}' G(\mathbf{r} - \mathbf{r}', \omega) o(\mathbf{r}') u_i(\mathbf{r}', \omega), \quad (17)$$

where the object function is

$$o(\mathbf{r}) \equiv [\delta(x - x_q) + \delta(x + x_q)]\delta(z - z_q), \quad (18)$$

i.e., two point scatterers separated by $2x_q$ at a distance of z_q from the transmitter/receiver. The incident pulse is described by the first derivative of a Gaussian, or “DOG” pulse, given by

$$p(t) = -(\sigma e^{1/2}) \frac{t - t_0}{\sigma^2} e^{-(t-t_0)^2/(2\sigma^2)}, \quad (19)$$

where $\sigma = 0.075$ ns. This choice was made so as to model the pulse of the actual LLNL MIR radar measurements described in Section VI. The DOG pulse and an LLNL MIR pulse measured from a

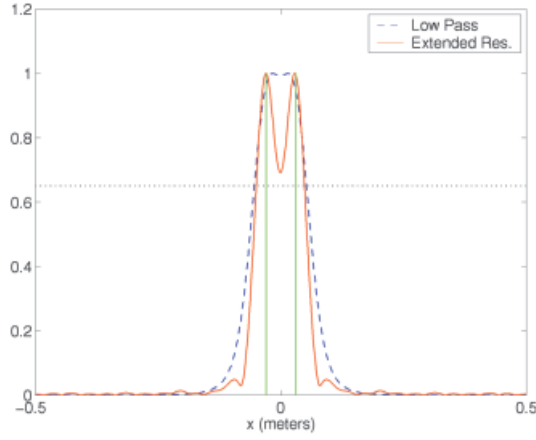


Figure 7. Two-point scatterer reconstruction slices. Slices through the low pass and extended resolution reconstructions at a constant $z = 20$ cm. The vertical lines indicate the actual scatterer location. The dotted horizontal line shows the threshold level of the reconstruction images.

reflection from a flat plate, along with their spectra, are presented in Figure 4. Antenna characteristics are not modeled, thus Eq. (19) is assumed to be the governing form of the incident field, a plane wave, given by

$$u_i(\mathbf{r}, \omega) \equiv A(\omega)e^{ik_0(\omega)z}, \quad (20)$$

with the amplitude, $A(\omega)$, given by the Fourier transform of the incident pulse of Eq. (19):

$$A(\omega) \equiv \int dt p(t)e^{-i\omega t}.$$

Combining Eqs. (17), (18), and (20), we have as our model

$$u_s(\mathbf{r}, \omega) = k_0^2(\omega)A(\omega)[G(x - x_q, z - z_q, \omega) + G(x + x_q, z - z_q, \omega)]e^{ik_0(\omega)z_q}. \quad (21)$$

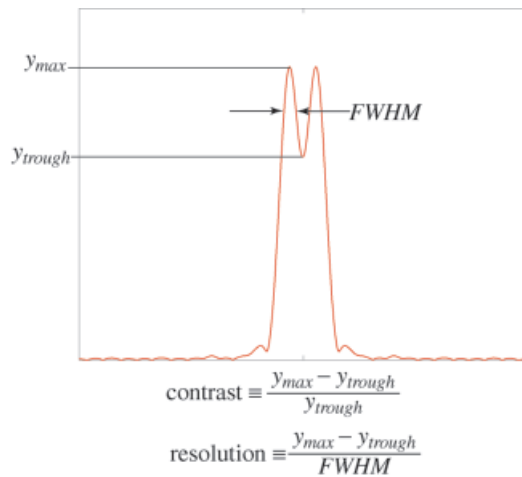


Figure 8. Figure of merit.

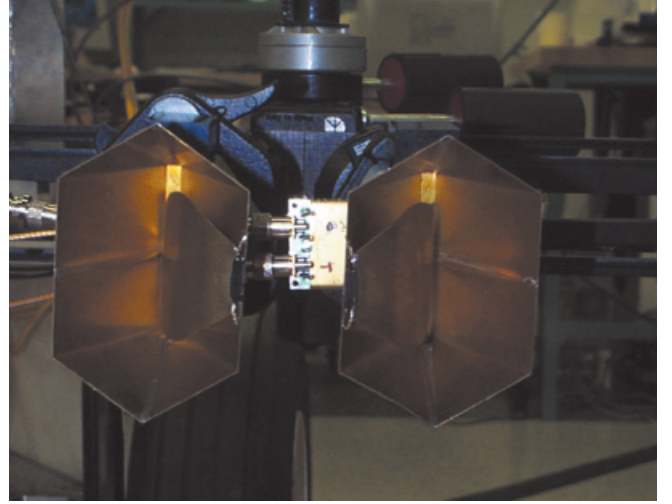


Figure 9. Photograph of the hexagonal LLNL MIR antennas.

We take our primary source and measurement line to be one and the same at $z \equiv 0$, i.e., we take $z_0 = z_M \equiv 0$ as our source/measurement line. Our measured scattered field is then

$$u_s(x, 0, \omega) = k_0^2(\omega)A(\omega)[G(x - x_q, -z_q, \omega) + G(x + x_q, -z_q, \omega)]e^{ik_0(\omega)z_q}. \quad (22)$$

Given $u_s(x, 0, \omega)$, the time domain measured scattered field is given by the inverse temporal Fourier transform:

$$u_s(x, 0, t) \equiv \frac{1}{2\pi} \int d\omega u_s(x, 0, \omega)e^{i\omega t}. \quad (23)$$

This field is shown in Figure 5 for $x_q = 3$ cm, i.e., for a scatterer separation of 6 cm. Their distance from the source/measurement line is $z_q = 20$ cm. The cross hairs superposed on the field indicate the location of the scatterers. The reconstructions are shown for the low pass and extended resolution cases in Figure 6 (a) and (b), respec-

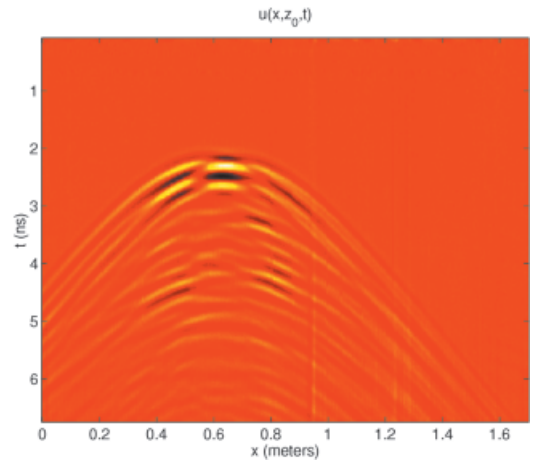


Figure 10. Measured field from two aluminum poles separated by 10 cm.

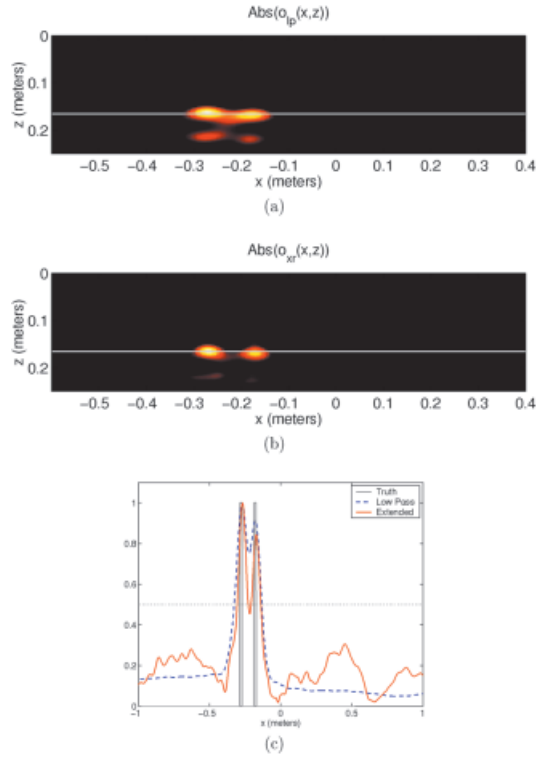


Figure 11. Two-pole reconstruction. (a) Low pass reconstruction. (b) Extended resolution reconstruction. (c) Slice through the reconstructions. The vertical gray bars indicate the pole location and width. The line through the reconstructions indicates the location of the slice.

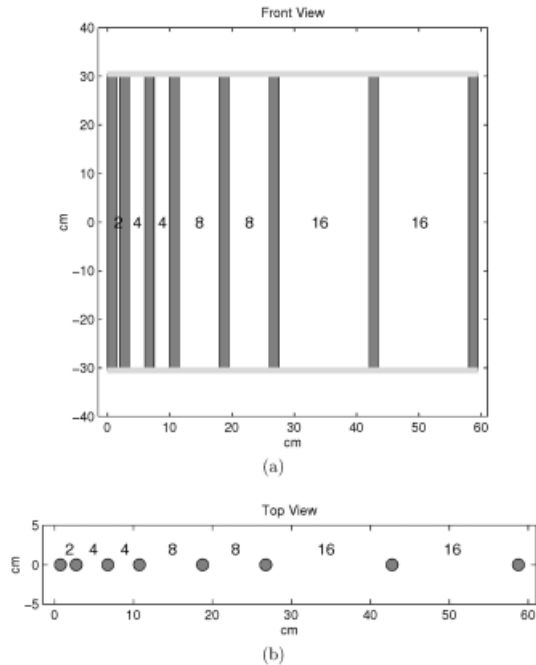


Figure 12. Resolution phantom schematic. The resolution phantom consists of eight aluminum bars 1.5 cm in diameter and approximately 60 cm in length held in place by Plexiglas staves at the top and bottom. The spacings between the bars are 2, 4, 4, 8, 8, 16, and 16 cm. (a) Front view. (b) Top view.



Figure 13. Photograph of the resolution phantom held by a vice.

tively. The value of the fractional decay parameter, τ , is 0.05. Again, the cross hairs superposed on the reconstructions indicate the location of the scatterers. The images have been thresholded such that all values below 65% of the maximum have been set to zero. The scatterers are indistinguishable in the low pass reconstruction. They are distinct in the extended resolution reconstruction. Slices through the reconstructions at a fixed value of $z \equiv z_q$ (Fig. 7) confirm this. The slices have been normalized to one. The vertical lines indicate the scatterer location and the dotted horizontal line shows the threshold level of the reconstruction images.

In order to attach a figure of merit to the reconstructions, we define the contrast and resolution between two peaks as:

$$\text{Contrast} \equiv \frac{y_{\max} - y_{\text{trough}}}{y_{\text{trough}}}, \quad (24)$$

$$\text{Resolution} \equiv \frac{y_{\max} - y_{\text{trough}}}{FWHM}, \quad (25)$$

where y_{\max} is the peak maximum, y_{trough} is the value of the trough between the two peaks, and $FWHM$ is the full width of a peak measured half way between the peak and the trough (Fig. 8).

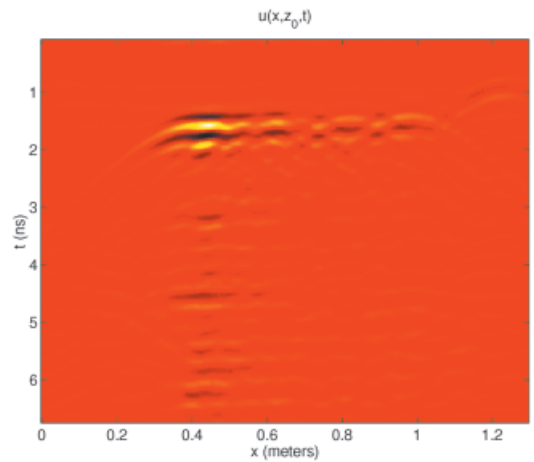


Figure 14. Measured field from buried resolution phantom.

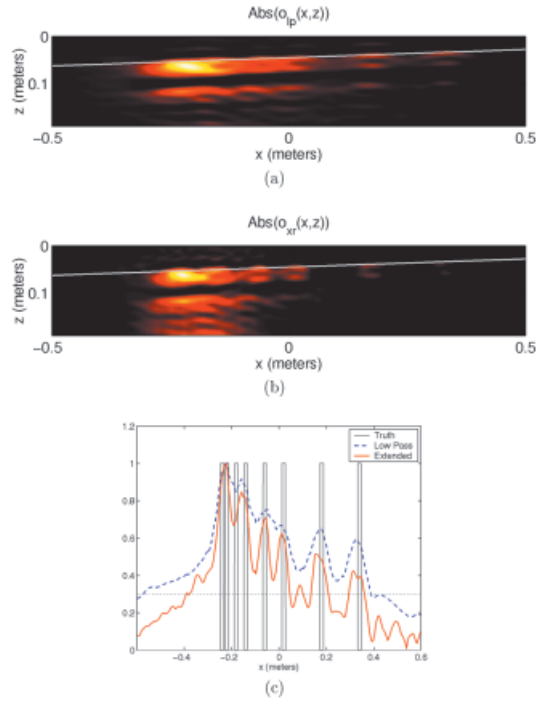


Figure 15. Buried resolution phantom reconstruction. (a) Low pass reconstruction. (b) Extended resolution reconstruction. (c) Slice through the reconstructions. The vertical gray bars indicate the pole location and width. The line through the reconstructions indicates the location of the slice.

Consider the limits of these figures of merit in a perfect reconstruction. y_{trough} and $FWHM$ would be identically zero. These are point scatterers of zero width. Thus, contrast and resolution would be infinite.

Measurements of y_{max} , y_{trough} , and $FWHM$ from the extended resolution reconstruction slice yield $y_{max} = 1$, $y_{trough} \approx 0.69$, and $FWHM \approx 3$ cm, for both peaks. We are unable to measure these values in the low pass case. The resulting contrast and resolution values are listed in Table I. Clearly, the extended resolution algorithm performs better than the low pass algorithm.

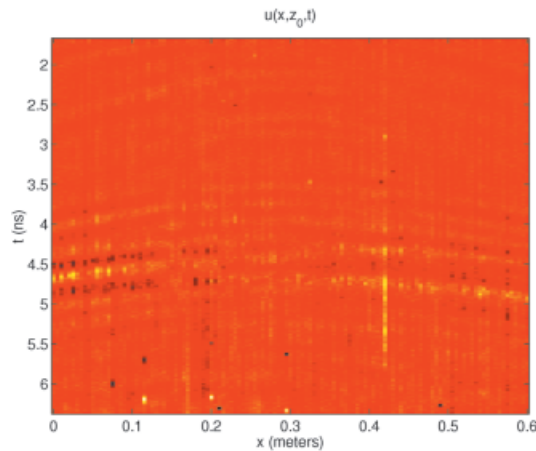


Figure 16. Measured field from buried M14 land mine.

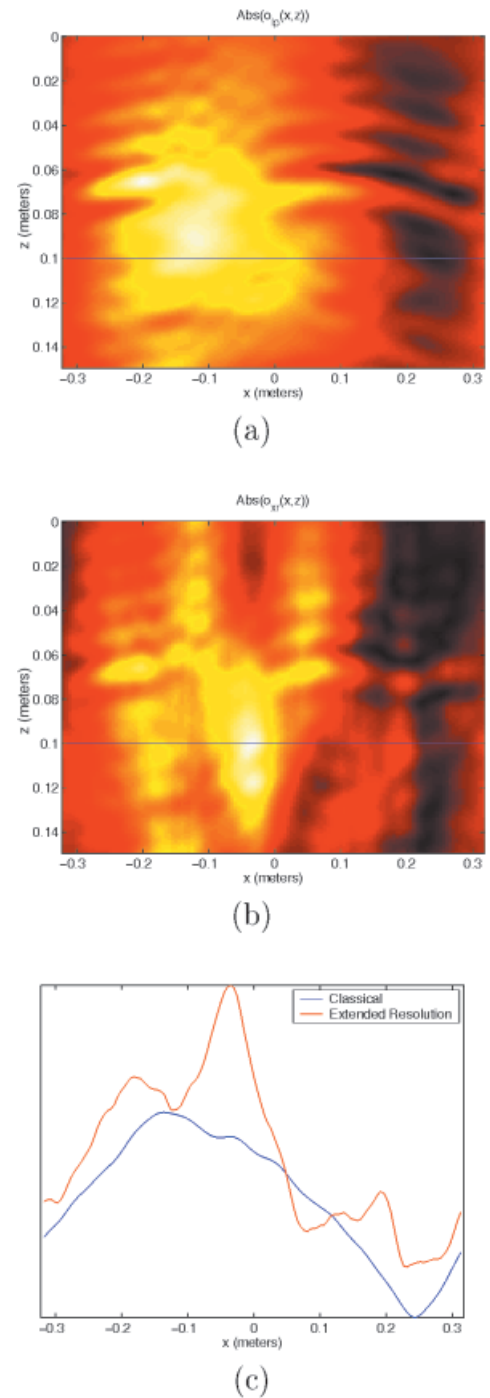


Figure 17. Buried M14 land mine reconstruction. (a) Low pass reconstruction. (b) Extended resolution reconstruction. (c) Slice through the reconstruction.

This test is used to confirm the theory and verify the inversion code, which is an exact inverse to the forward model of Eq. (21) up to the usual numerical limitations. In the next section, we apply the algorithm to the reconstruction of real targets using actual wideband radar data measurements.

VI. APPLICATION TO REAL DATA

We use experimental results to show that the reconstruction algorithm presented in Section III achieves superresolution, i.e., resolu-

Table I. Two-point scatterer reconstruction figure of merit.

	Low Pass	Extended Resolution	Perfect Reconstruction
Contrast	0	0.45	∞
Resolution	0	10.3	∞

tion beyond the classical limit. We confirm this by comparing the reconstructions using exclusively the propagating field information (the classically resolution limited or low pass reconstructions) with those resulting from our algorithm, which uses both the propagating and evanescent fields (the extended resolution reconstructions). We operate in a reflection mode with the transmitter/receiver colocated in the measurement plane. For convenience, we take this plane to be zero, i.e., $z_0 = z_M \equiv 0$. We collected wideband microwave experimental data from two aluminum poles, a buried aluminum resolution phantom, and finally, a buried inert, plastic M14 antipersonnel land mine.

We describe the LLNL MIR that collected the experimental data. We present the measured field results and reconstructions of two circular cylinder aluminum scatterers, the buried aluminum resolution phantom, and the M14 antipersonnel land mine, respectively, from a multimono-static scan taken with the LLNL MIR.

A. LLNL MIR. The experimental results were acquired using the LLNL MIR (Azevedo and McEwan, 1996; Azevedo et al., 1996; Lawrence Livermore National Laboratory, 1996). The particular type of MIR used was the range finder.

The MIR range finder is a fundamentally different type of radar that was invented and patented by the LLNL (1996). It is a pulsed radar like other ultrawide band radars, but it emits much shorter pulses than most because it is constructed out of a small number of common electronic components. It is also compact and inexpensive.

A unique feature of the MIR is the pulse generation circuitry. Although it is small and inexpensive, it had never before been considered in radar applications. Each pulse is less than a billionth of a second and each MIR emits about 2 million of these pulses per second. Pulse repetition rates are coded with random noise to reduce the possibility of interference from other radars. Each pulse is “self-tuned.” There are three advantages of the short pulse width:

1. With pulses so short, the MIR operates across a wider band of frequencies than a conventional radar, giving high resolution and accuracy, but also making it less susceptible to interference from other radars.
2. Because current is only drawn during this short pulse time and the pulses are infrequent, there are extremely low power requirements. For example, one type of MIR unit can operate for years on a single AA battery.

Table II. Two aluminum pole figure of merit parameters.

	Low Pass	Extended Resolution
y_{max1}	1	1
y_{max2}	0.91	0.84
y_{trough}	0.75	0.46
$FWHM1$	0.045	0.048
$FWHM2$	0.040	0.045

Table III. Two aluminum pole reconstruction figure of merit.

	Low Pass	Extended Resolution
Contrast 1	0.33	1.17
Contrast 2	0.21	0.83
Resolution 1	5.56	11.25
Resolution 2	4.00	8.44

3. The microwave power emitted by the pulses is at microwatt levels and, therefore, medically safe.

Figure 9 shows a photograph of two hexagonal MIR antennas that were used to collect the data presented here. In order to operate in a multimono-static mode, the antennas were placed as close as possible without physically touching. One antenna served as a transmitter, the other as a receiver.

The MIR range finder has a typical 3-GHz bandwidth with a center frequency of 3 GHz (Azevedo et al., 1996) pulse. As stated above, it operates with a pulse repetition frequency (PRF) of 2 MHz. Each pulse is range gated back to fill in a single time bin. By sweeping the range gate over time, a complete time series is acquired. Figure 4 shows a typical MIR range finder pulse along with its Fourier spectrum. Also shown is the DOG pulse of Eq. (19), which is used to model the MIR pulse. The DOG pulse was chosen because it closely approximates the MIR pulse in both the temporal and spectral domains.

The reconstruction algorithm requires the spectrum of the incident pulse. We were unable to measure a sufficiently noise-free MIR to use in the reconstruction of the real MIR data. In its place, we used the spectrum of the DOG pulse.

B. MIR Scan of Two Aluminum Poles. An MIR scan of two aluminum poles was performed to test the reconstruction code on real wideband microwave data. The poles were 1.5 cm in diameter and were separated by approximately 10 cm. The experiment was performed in air. They were located approximately 31.5 cm in front of the radar. From the spectrum shown in Figure 4, we see that the MIR pulse has a peak of about 2 GHz. This corresponds to a free space wavelength of approximately 15 cm. Thus, the poles are located about two peak wavelengths away from the radar, within the extreme limit of the near field.

A background scan was performed (in the absence of the poles) and subtracted from the scan of the poles. This eliminated reflections from other scatterers within the room as well as reduced the noise. There are 341 multimono-static locations separated by 5 mm. The measured field is shown in Figure 10. We observe multiple reflections from a wall behind the poles arriving after the direct reflection from the poles. This reconstructs as multiple images of the poles farther from the receiver line.

Table IV. Resolution phantom figure of merit parameters.

	Low Pass	Extended Resolution
y_{max1}	0.65	0.51
y_{max2}	0.59	0.42
y_{trough}	0.37	0.21
$FWHM1$	0.08	0.06
$FWHM2$	0.07	0.06

Table V. Resolution phantom reconstruction figure of merit.

	Low Pass	Extended Resolution
Contrast 1	0.76	1.43
Contrast 2	0.59	1.00
Resolution 1	3.50	5.00
Resolution 2	3.14	3.50

The reconstructions are shown in Figure 11. The value of τ is 0.10. Although the poles are distinguishable in both the low pass and extended resolution reconstructions, the latter shows improved resolution as expected. We confirmed this by computing the contrast and resolution figures of merit for the two poles. We label the left-hand pole as 1 and the right-hand pole as 2. The parameters used in computing the figures of merit are listed in Table II. The contrast and resolution numbers are listed in Table III. The extended resolution reconstruction shows a 250% contrast increase for pole 1 and a 300% increase for pole 2. Both poles show an approximate 100% increase in resolution. These are excellent results given the limitation (Born approximation) of the reconstruction algorithm, which was not designed to operate in a highly scattering environment. The quality of the extended resolution reconstruction demonstrates the importance of including the evanescent fields.

C. Resolution Phantom. An aluminum resolution phantom was designed to test the resolution limits of the LLNL MIR. The phantom consists of eight circular cylinder bars 1.5 cm in diameter and approximately 60 cm in length, held in place by Plexiglas staves at the top and bottom. The spacings between the bars are 2, 4, 4, 8, 8, 16, and 16 cm. A schematic of the resolution phantom is shown in Figure 12 and a photograph is shown in Figure 13.

We used the LLNL MIR to scan the resolution phantom when buried in dry sand 3 cm below the surface. We estimate the relative permittivity of sand to be approximately 3. The sand was in a sandbox approximately 1.5 m² in surface area and 60 cm deep. The radar was 11 cm above the surface.

A background scan was taken of the sandbox and subtracted from the resolution phantom scan. This eliminated reflections from other scatterers within the room and sand box, as well as reduced the noise. There are 260 multimonostatic locations separated by 5 mm. The measured field is shown in Figure 14. Visible in the field are multiple returns from the bottom of the box. These reconstruct as multiple images of the phantom.

The reconstructions are shown in Figure 15. The value of τ is 0.10. The extended resolution algorithm succeeded in resolving the 8-cm pair of poles. The low pass algorithm was only able to resolve the poles separated by 16 cm.

Using the reconstruction slices of Figure 15 (c), we list the figure of merit parameters and derived figures of merit in Tables IV and V, respectively, for the right-hand pair of poles. The left pole is labeled 1, the right is 2. We see an 88% increase in contrast for pole 1 and a 70% increase for pole 2. There is a 43% increase in resolution for pole 1 and an 11% increase for pole 2.

These are remarkable results considering the permittivity contrast among the air, sand, and phantom. The permittivity changes from one material to the next lie far outside the Born approximation of the model.

D. Buried Land Mine. An inert, plastic M14 land mine was buried just below the surface in dry sand. The M14 is a cylindrical

antipersonnel mine, approximately 6 cm in diameter and 5 cm high, and this would be its typical placement. We collected LLNL MIR data with the antennas approximately 9 cm above the surface.

Although most of the quantitative ground truth is missing for this data set, we include it as a practical demonstration of the improvement offered by the extended resolution algorithm. The background-removed measured backscattered field is shown in Figure 16. The low pass and extended resolution reconstructions are presented in Figure 17. The mine shows a better resolution in the extended resolution reconstruction than in the low pass reconstruction. This is supported by the slice through the reconstruction shown in Figure 17(c). As a final comment, we suspect the LLNL MIR antennas, as shown in Figure 9 may have been separated by several centimeters when this data set was collected. We believe this resulted in the spatial migration of the object center of mass to the right in the extended resolution reconstruction with respect to the low pass reconstruction.

VII. CONCLUSIONS

We extended the Porter-Bojarski theory to include the evanescent field in the forward scattering model, providing a basis for incorporating it in the inversion process. We specialized our model to a reflection mode, multimonostatic, wideband wave probing system and developed a tomographic reconstruction algorithm. After verifying the basic code operation, we collected wideband radar data using the LLNL MIR from two parallel aluminum poles, an aluminum resolution phantom buried in dry sand, and a buried, inert, plastic M14 antipersonnel land mine. We compared the reconstruction results of our code with those of a classical diffraction tomography code that does not incorporate the evanescent field. The reconstructions from our code showed increased resolution and contrast over the classical code. The results indicate the importance of including the evanescent field in the reconstruction. It is remarkable that improved contrast and resolution are achieved even in these highly scattering cases that violate the Born approximation model. Because this algorithm makes use of the evanescent fields, improved reconstructions can be achieved simply by moving the antennas closer to the scattering object. We do offer a word of caution, however, for wet soil environments. In these highly absorbing conditions, there is limited depth penetration and thus backscatter in both the propagating and evanescent spectral regions. Further research must be performed in order to achieve practical reconstructions under these conditions.

The theoretical development summarized here and presented in full detail in Lehman (2000) are for arbitrary dimensionality. Although the proof-of-principle and examples are given in 2D for simplicity, we believe the extended resolution algorithm can be extended to three dimensions with minor modifications. Certainly, we may “extend” the dimensionality by stacking a set of 2D reconstructions.

ACKNOWLEDGMENTS

The author thanks Dr. Stephen Azevedo and Tom Rosenbury for the use of the LLNL MIR; Ming Liu, Pat Welsh, and Mark Vigars for their assistance with the MIR and instruction on how to use the controlling software; and Drs. James Candy and David Chambers for reviewing and commenting on the total field theory.

REFERENCES

M.P. André, H.S. Janée, P.J. Martin, G.P. Otto, B.A. Spivey, and D.A. Palmer, High-speed data acquisition in a diffraction tomography system

- employing large-scale toroidal arrays, *Int J Imaging Syst Technol* 8 (1997), 137–147.
- M.P. André, P.J. Martin, G.P. Otto, L.K. Olson, T.K. Barrett, B.A. Spivey, and D.A. Palmer, A new consideration of diffraction computed tomography for breast imaging: Studies in phantoms and patients, *Acoustical Imaging* 21 (1995), 379–390.
- S.G. Azevedo and T.E. McEwan, Micropower impulse radar, Technical Report UCRL-52000-96-1/2, Science and Technology Review, Lawrence Livermore National Laboratory, Livermore, CA, 1996, pp. 16–29.
- S.G. Azevedo, T.E. McEwan, and J.P. Warhus, Microradar development, Technical Report UCRL-53868-95, Engineering Research, Development and Technology: Thrust Area Report, Lawrence Livermore National Laboratory, Livermore, CA, 1996, pp. 6–17.
- M.J. Berggren, S.A. Johnson, B.L. Carruth, W.W. Kim, F. Stenger, and P.L. Kuhn, Performance of fast inverse scattering solutions for the exact helmholtz equation using multiple frequencies and limited views, *Acoustical Imaging* 15 (1986a), 193–201.
- M.J. Berggren, S.A. Johnson, B.L. Carruth, W.W. Kim, F. Stenger, and P.L. Kuhn, Ultrasound inverse scattering solutions from transmission and/or reflection data, *SPIE Phys Eng Comput Multidimen Imaging Process* 671 (1986b), 114–121.
- R.O. Bohbot, D. Lesselier, and B. Duchêne, A diffraction tomographic algorithm for eddy current imaging from anomalous fields at fictitious imaginary frequencies, *Inverse Problems* 10 (1994), 109–127.
- J.C. Bolomey and C. Pichot, Microwave tomography: From theory to practical imaging systems, *Int J Imaging Syst Technol* 2 (1990), 144–156.
- M. Born and E. Wolf, *Principles of optics* (7th ed.), Cambridge University Press, Cambridge, England, 1999.
- G.C. Carter (Editor), *Coherence and time delay estimation: An applied tutorial for research, development, test, and evaluation engineers*, IEEE Press, Piscataway, NJ, 1993.
- R.W. Deming, New tomographic imaging methods for geophysical and medical applications, PhD thesis, Northeastern University, Boston, MA, 1996.
- R.W. Deming and A.J. Devaney, Diffraction tomography for multi-monostatic ground penetrating radar imaging, *Inverse Problems* 13 (1997), 29–45.
- A.J. Devaney, A filtered backpropagation algorithm for diffraction tomography, *Ultrasonic Imaging* 4 (1982), 336–350.
- O. Dorn, H. Bertete-Aguirre, J.G. Berryman, and G.C. Papanicolaou, A nonlinear inversion method for 3D electromagnetic imaging using adjoint fields, *Inverse Problems* 15 (1999), 1523–1558.
- B.R. Hunt, Super-resolution of images: Algorithms, principles, performance, *Int J Imaging Syst Technol* 6 (1995), 297–304.
- N. Joachimowicz, C. Pichot, and J.-P. Hugonin, Inverse scattering: An iterative numerical method for electromagnetic imaging, *IEEE Trans Antennas Propag* 39 (1991), 1742–1752.
- S.A. Johnson and M.L. Tracy, Inverse scattering solutions by a sinc basis, multiple source, moment method—Part I: Theory, *Ultrasonic Imaging* 5 (1933), 361–375.
- A.C. Kak and M. Slaney, *Principles of computerized tomographic imaging*, IEEE Press, Piscataway, NJ, 1988.
- K.J. Langenberg, “Applied inverse problems for acoustic, electromagnetic and elastic wave scattering,” *Basic methods of tomography and inverse problems*, P.C. Sabatier (Editor), Malvern Physics Series, Adam Hilger, Bristol, UK, 1987, pp 125–467.
- Lawrence Livermore National Laboratory, MIR technology overview, <http://lasers.llnl.gov/lasers/idp/mir/mir.html> 1996.
- S.K. Lehman, Superresolution of buried objects in layered media by near-field electromagnetic imaging, PhD thesis, University of California at Davis, 2000.
- J.E. Mast, Microwave pulse-echo radar imaging for the nondestructive evaluation of civil structures, PhD thesis, University of Illinois, Urbana-Champaign, 1993.
- F. Natterer and F. Wubbeling, A propagation-backpropagation method for ultrasound tomography, *Inverse Problems* 11 (1995), 1225–1232.
- A. Schatzberg and A.J. Devaney, Imaging with evanescent waves in diffraction tomography, *Inverse Problems Scattering Imaging SPIE* 1767 (1992), 260–269.
- A. Schatzberg and A.J. Devaney, Super-resolution in diffraction tomography, *Inverse Problems* 8 (1992b), 149–164.
- J.W. Wiskin, D.T. Borup, and S.A. Johnson, Inverse scattering from arbitrary two-dimensional objects in stratified environments via a green’s operator, *J Acoustical Soc Am* 102 (1997), 853–864.